JVSTA Journal of Vacuum Science & Technology A

Atomic bonding effects in annular dark field scanning transmission electron microscopy. I. Computational predictions

Michael L. Odlyzko, Burak Himmetoglu, Matteo Cococcioni, and K. Andre Mkhoyan

Citation: Journal of Vacuum Science & Technology A **34**, 041602 (2016); doi: 10.1116/1.4954871
View online: http://dx.doi.org/10.1116/1.4954871
View Table of Contents: http://scitation.aip.org/content/avs/journal/jvsta/34/4?ver=pdfcov
Published by the AVS: Science & Technology of Materials, Interfaces, and Processing

Atomic bonding effects in annular dark field scanning transmission electron microscopy. I. Computational predictions

Michael L. Odlyzko
Department of Chemical Engineering and Materials Science, University of Minnesota, Minneapolis, Minnesota 55455

Burak Himmetoglu
Department of Chemical Engineering and Materials Science, University of Minnesota, Minneapolis, Minnesota 55455 and Materials Department, University of California, Santa Barbara, California 93106

Matteo Cococcioni
Department of Chemical Engineering and Materials Science, University of Minnesota, Minneapolis, Minnesota 55455 and Theory and Simulations of Materials, National Centre for Computational Design and Discovery of Novel Materials, École polytechnique fédérale de Lausanne (EPFL), CH-1015 Lausanne, Switzerland

K. Andre Mkhoyan[a)]
Department of Chemical Engineering and Materials Science, University of Minnesota, Minneapolis, Minnesota 55455

(Received 31 May 2016; accepted 9 June 2016; published 30 June 2016)

Annular dark field scanning transmission electron microscopy (ADF-STEM) image simulations were performed for zone-axis-oriented light-element single crystals, using a multislice method adapted to include charge redistribution due to chemical bonding. Examination of these image simulations alongside calculations of the propagation of the focused electron probe reveal that the evolution of the probe intensity with thickness exhibits significant sensitivity to interatomic charge transfer, accounting for observed thickness-dependent bonding sensitivity of contrast in all ADF-STEM imaging conditions. Because changes in image contrast relative to conventional neutral atom simulations scale directly with the net interatomic charge transfer, the strongest effects are seen in crystals with highly polar bonding, while no effects are seen for nonpolar bonding. Although the bonding dependence of ADF-STEM image contrast varies with detector geometry, imaging parameters, and material temperature, these simulations predict the bonding effects to be experimentally measureable. © *2016 American Vacuum Society*.
[http://dx.doi.org/10.1116/1.4954871]

I. INTRODUCTION

Conventional implementations of multislice[1] transmission electron microscopy (TEM) image simulation[2,3] model the electrostatic potential of a solid as that of a collection of unbonded neutral atoms; this approximation is known as the independent atom model (IAM). It is known that failure to account for bonding introduces significant errors in calculations of low-angle electron scattering,[4] accounting for the power of quantitative convergent-beam electron diffraction for valence charge density determination.[5,6] Accordingly, several studies have also examined the sensitivity of bright-field conventional TEM imaging to bonding orbital charge density, showing that valence charge redistribution due to bonding significantly affects image contrast for thin oxide crystals[7,8] and two-dimensional materials.[9] Differential phase contrast scanning TEM (STEM) has also been used to detect charge transfer in highly polar crystals.[10,11] However, no published study has considered the sensitivity of other standard TEM imaging modes, including annular dark field (ADF) STEM, to valence charge distribution.

Among these modes, the high-angle ADF (HAADF) variant of ADF-STEM is especially interesting, being an approximately incoherent imaging mode wherein image intensity originates from the high-angle scattering of fast electrons from positively charged atomic ion cores.[12,13] The primary advantages of HAADF-STEM imaging are robust direct proportionality between HAADF-STEM image intensity and the mass-thickness of the specimen,[14] as well as the possibility of efficient parallel electron-energy-loss spectroscopy (EELS) of the electrons transmitted past the detector. Advances in electron optics for aberration correction[15,16] allow HAADF-STEM imaging with sub-Angstrom resolution, readily resolving very narrowly spaced atomic columns.[17,18] Such imaging is widely regarded as insensitive to bonding because valence charge redistribution should not alter the high-angle scattering of probe electrons.

For a STEM probe placed near an atomic column, beam intensity focuses onto the column and oscillates with depth, an effect known as channeling.[19,20] Simulations show that on-column channeled intensity can be highly sensitive to atomic number (Z), crystal orientation, and imaging conditions.[21] Careful analysis of ADF-STEM image simulation further shows that both on-column channeling and intercolumn beam spreading determine the thickness-dependent

[a)]Author to whom correspondence should be addressed; electronic mail: mkhoyan@umn.edu

image contrast in zone-axis-oriented crystals.[22–24] Although challenging to measure, both on-column channeling[25] and intercolumn beam spreading[26] have been characterized experimentally in zone-axis-oriented crystals. The coherent low-angle scattering that determines channeling and beam-spreading behavior is known to be bonding-sensitive, but this dependence has not been examined explicitly.

Including valence charge redistribution due to bonding may change both the propagation of a focused electron beam through the sample and the strength of high-angle scattering from individual atoms in the column, both of which ultimately affect ADF-STEM image contrast. To begin understanding the effect of bonding on the ADF-STEM imaging of crystals, this study surveys the effects of bonding model, atomic composition, incident probe, detector geometry, and thermal vibrations in bonding-inclusive multislice simulations. The results of the study not only refine the analysis of ADF-STEM imaging of perfect single crystals, but also point toward an approach for simulating imaging of defects that locally distort the bonding states of atoms, such as ordered point defects[27] and interfaces[28] in ceramic materials.

II. METHODS

HAADF-STEM images of light-element single crystals were simulated using the multislice method as implemented by the TEMSIM code[29] developed by Kirkland. The crystals studied were diamond carbon (d-C), cubic boron nitride (c-BN), wurtzite boron nitride (w-BN), wurtzite aluminum nitride (AlN), wurtzite beryllium oxide (BeO), halite magnesium oxide (MgO), halite lithium fluoride (LiF), and halite sodium fluoride (NaF). These materials were chosen to compare bonding effects across differences in crystal structure, bond length, bond polarity, and bond valency, surveyed in Table I.

To determine the effects of bonding using computational methods, three different bonding models were used: the IAM, the bonded crystal model (BCM), and the fully ionized model (FIM). In IAM, the charge density of the solid was calculated as the superposition of the charge densities of independent neutral atoms. In BCM, the charge density of the solid was calculated as the superposition of atomic ion-core charge densities with valence charge densities calculated by density functional theory (DFT). In FIM, the charge density of the solid was calculated as the superposition of the charge densities of independent full-valence-shell ions. Although it is BCM that expressly emulates the bonding of real solids, it is instructive to compare it to the hypothetical extremes of nonexistent (IAM) and complete (FIM) charge transfer. Consideration of these extremes is also motivated by the fact that the bonding at crystal defects may either increase or decrease the degree of bonding-induced charge transfer relative to the bulk, causing the bonding to locally veer away from bulk BCM character toward something more like either bulk FIM or bulk IAM. Because IAM is the standard mode of simulation, it has been treated as the reference against which the other models are compared.

All charge densities were calculated using the Quantum ESPRESSO (Ref. 30) DFT software package. Single-atom charge density calculations (used for core orbital charge densities of all models, as well as valence charge densities of both IAM and FIM) were performed on a 2000-point logarithmic radial grid out to 0.5 nm, using the PBE-GGA (Ref. 31) functional, which was checked to give charge densities consistent with those calculated using the LDA (Ref. 32) functional. Valence charge density calculations for the BCM model were performed using the LDA functional.

To produce inputs for multislice simulation, unit cell charge densities were transformed to electrostatic potentials using periodic boundary conditions,[33] sectioned into slices centered on atomic planes, and integrated over slice thickness to produce exact projected potentials that could serve as inputs for multislice simulations without thermal diffuse scattering (TDS). To perform TDS-inclusive calculations, the exact projected potentials were approximately parameterized as sums of radially symmetric gaussians and Bessel functions of the first kind,[29] allowing on-the-fly calculation of frozen-phonon configurations by TEMSIM for each bonding model. Sums of three Gaussians and three Bessel functions centered on each atom were used to parameterize individual atomic potentials by fitting the exact ground state projected potentials calculated using each bonding model. This is the same form of parametrization employed by TEMSIM multislice code.[29] To ensure accurate TDS-inclusive simulations, RMS thermal vibration values were determined from the experimental diffraction literature. It should be noted that the procedure of radially averaging the bonding effect in a case of BCM model produces more conservative approximation relative to more accurate directional representation of the bonds. As a result, it should be expected that the effects of bonding on probe channeling and ADF-STEM imaging in actual crystal are more prominent then ones presented here.

Crystals were analyzed at zone axes with each column containing only one type of atom [⟨100⟩ for diamond cubic

TABLE I. Comparison of the crystal structure, bond length, bond polarity, and bond valency of the crystals studied. Crystals increase in bond polarity from left to right.

Property	d-C	c-BN	w-BN	AlN	BeO	MgO	LiF	NaF
Crystal structure	Diamond $Fd\bar{3}m$	Zinc blende $F\bar{4}3m$	Wurtzite $P6_3mc$	Wurtzite $P6_3mc$	Wurtzite $P6_3mc$	Halite $Fm\bar{3}m$	Halite $Fm\bar{3}m$	Halite $Fm\bar{3}m$
Bond length (nm)	0.154	0.156	0.157	0.190	0.165	0.148	0.143	0.163
Pauling ΔX	0.00	1.00	1.00	1.43	1.87	2.13	3.00	3.05
Formal valency	0	±3	±3	±3	±2	±2	±1	±1

TABLE II. Rayleigh criterion diffraction-limited resolution in (nm) of the STEM probes considered in this study. Each value corresponds to the radius of the central Airy disk formed in each condition, which is approximately equal to the full-width-at-half-maximum (FWHM) of an aberration-free probe.

	Probe convergence angle (mrad)		
Beam energy (keV)	15	25	35
60	0.198	0.119	0.085
100	0.151	0.091	0.065
200	0.102	0.062	0.044

crystals, ⟨110⟩ for halite cubic, and ⟨$\bar{2}$110⟩ for wurtzite crystals]. Probe and transmission functions were each calculated on a 1024×1024 pixel grid, with supercell edge lengths varying over 2.29–4.35 nm across all of the materials studied. Probe energies ranging 60–200 keV, convergence semiangles ranging 15–35 mrad, ADF detector inner angles ranging 40–200 mrad (default HAADF detector geometry used a 60 mrad inner angle and 200 mrad outer angle, but other combinations of inner and outer angles were also studied), and material temperatures (T = 77 and 300 K) in addition to TDS-free case were all considered in examining the effects of bonding on ADF-STEM imaging. For reference, the diffraction-limited resolution of each simulated probe is listed in Table II, calculated according to the Rayleigh criterion.

Effects of finite source size were generally neglected, and when included were calculated as the convolution of a simulated image with a two-dimensional Gaussian of specified FWHM. All image intensities are represented as scattered currents normalized to the incident beam current. Channeling and beam-spreading calculations are calculated as normalized fluxes (i.e., beam current at that pixel divided by the product of incident beam current and the pixel area; neglecting attenuation of current due to absorption, the integral of the normalized flux over the supercell area at any slice is unity).

III. RESULTS AND DISCUSSION

A. HAADF imaging

Owing to its predominant selection of incoherently scattered beams and optimal complementarity to core-loss EELS, HAADF-STEM imaging is a widely used imaging mode that approximately offers simple "Z-contrast." In reality, on-column channeling, beam spreading, and TDS all significantly affect HAADF-STEM image contrast in zone-axis-oriented crystals.

To isolate the essential effect of bonding on ADF-STEM imaging, we first consider this HAADF-STEM imaging mode (where bonding should be less influential than lower-inner-angle ADF-STEM modes, due to exclusion of coherent zero-order Laue zone scattering) in the absence of TDS effects. As shown in Sec. III E, where the results from crystals with and without TDS are compared, simulations for crystals with no atomic vibrations (TDS-free crystals) qualitatively describes all the effects of bonding on probe channeling and ADF-STEM imaging. More discussion on validity of using TDS-free crystal as a model for qualitatively understanding probe channeling, imaging and diffraction in TEM can be found in Ref. 29. A very useful means for analyzing thickness-dependent HAADF-STEM imaging of crystals is plotting a HAADF intensity linescan as a function of depth (henceforth termed "x-z profiles"). Plotting x-z profiles for a 100 keV probe with 25 mrad convergence in ⟨$\bar{2}$110⟩-oriented AlN (Fig. 1) shows that bonding produces differences in intensity as a function of depth, and that this depth-evolution varies with bonding model.

Quantitative comparison of those x-z profiles (Fig. 2) reveals significant differences between IAM and BCM simulations, and still more pronounced differences between IAM and FIM; this is readily seen both when differences are taken on an absolute scale $\Delta = I_{\text{bonded}} - I_{\text{IAM}}$ [Fig. 2(a)] and when they are normalized to the IAM intensity value and reported as the percentage $100 \times (I_{\text{bonded}} - I_{\text{IAM}})/I_{\text{IAM}}$ [Fig. 2(b)]. The normalized differences highlight the effect of bonding in proportion to the IAM image intensity at any thickness, and thus are used in all of the following x-z profile comparisons.

A systematic examination for a 100 keV probe with 25 mrad convergence shows clearly that both ⟨$\bar{2}$110⟩-oriented wurtzite crystals (Fig. 3) and ⟨110⟩-oriented halite crystals (Fig. 4) have HAADF-STEM image contrast affected by

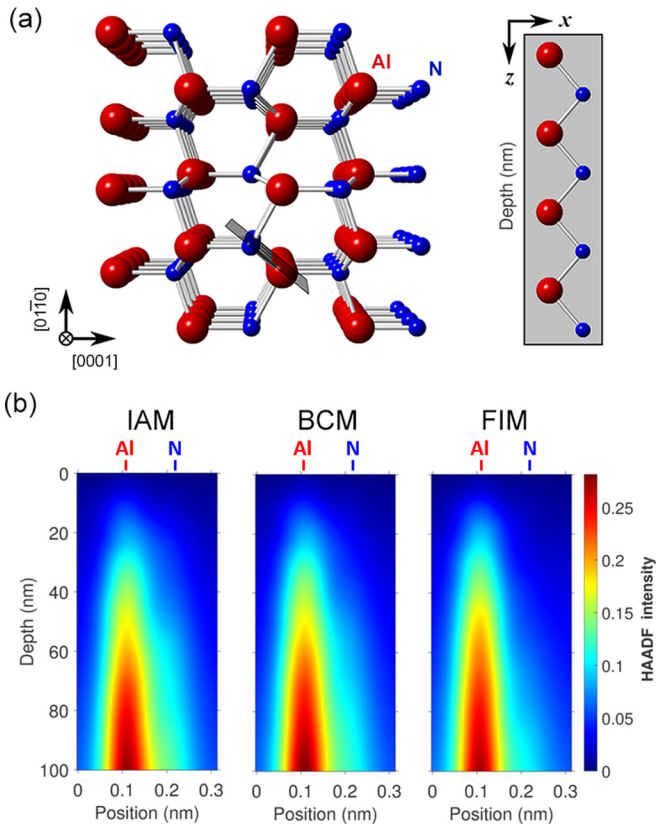

FIG. 1. (Color online) For an x-z profile of the HAADF signal along the indicated line in ⟨$\bar{2}$110⟩-oriented AlN (a), HAADF-STEM image simulations of a 25 mrad 100 keV probe using each bonding model (b) give slightly different depth-dependent contrast, most visible as a weakening of the N column shoulder as a function of increasing charge transfer.

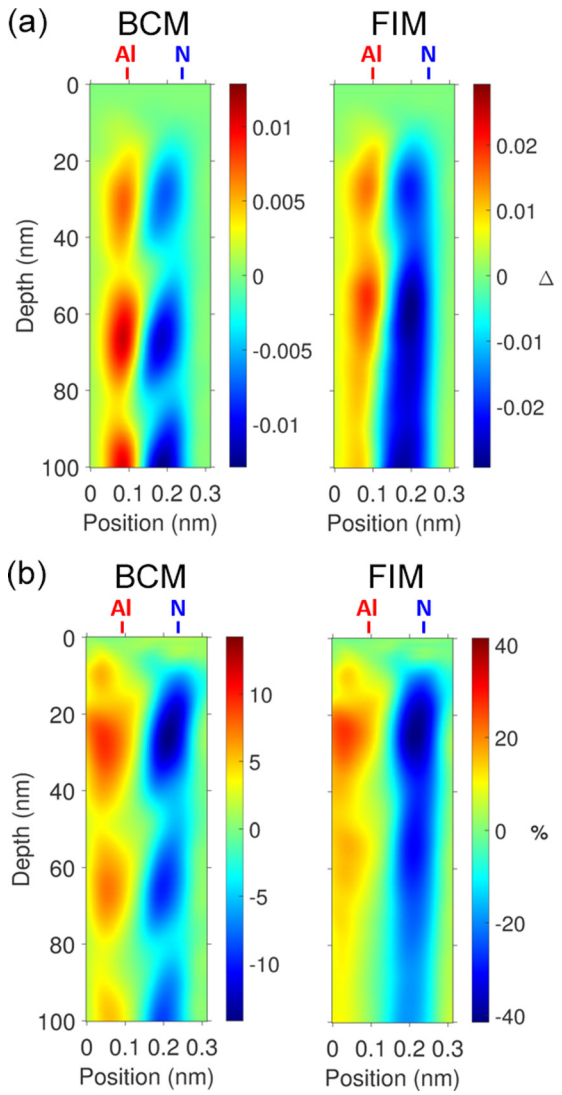

FIG. 2. (Color online) Quantitative comparisons of HAADF linescans of a 100 keV probe with 25 mrad convergence in $\langle\bar{2}110\rangle$-oriented AlN: (a) raw difference between bonding-inclusive and IAM x-z profiles and (b) difference normalized to IAM x-z profile.

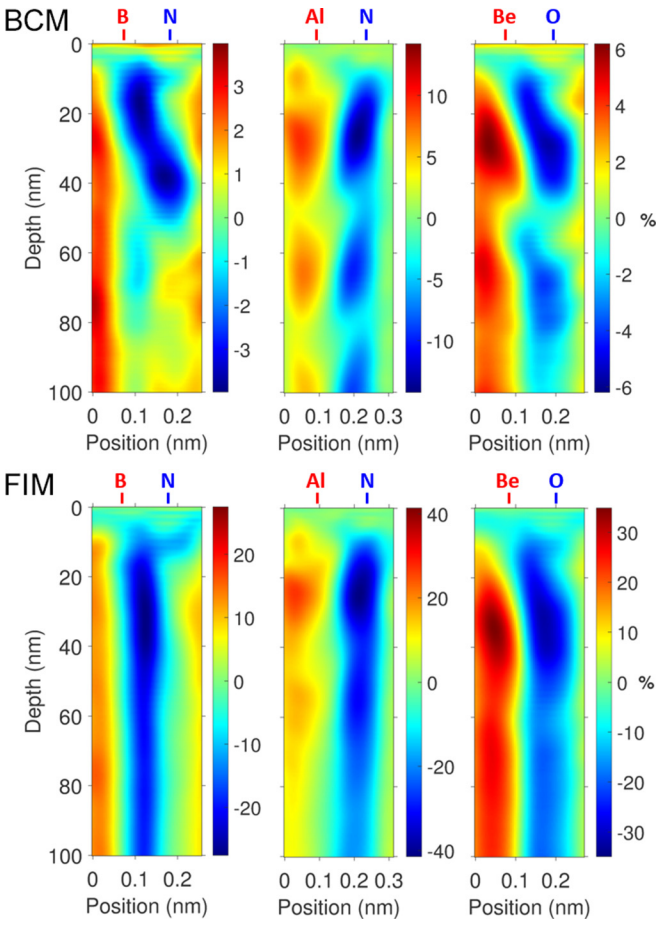

FIG. 3. (Color online) Normalized HAADF x-z profile differences of (a) BCM and (b) FIM bonding models relative to IAM reference, for $\langle\bar{2}110\rangle$-oriented wurtzite crystals. Crystals increase in polarity from left to right. BCM vs IAM differences are weaker than FIM vs IAM.

polar bonding. Normalized differences are strongest in between neighboring columns but are also large on the columns themselves. In general, cation columns increase in intensity while anion columns decrease, although the B column in w-BN serves as an exception. In all cases, the magnitude of bonding effects is highly depth-sensitive. Cation signal increases were found to be as large as 10% and anion signal decreases as large as 15%, relative to IAM, for BCM models. For FIM models, the maximum changes relative to IAM were a 35% cation signal increase and a 40% anion signal decrease.

The critical effect of charge transfer on HAADF-STEM imaging can be seen more definitively by comparing BCM calculations with varying degrees of charge transfer between atoms. By artificially changing the electronic potential energy on Al in AlN, the bond polarity can be tuned (increasing the electron potential energy on the cation increases polarity, reducing the energy reduces polarity). Normalized differences relative to the IAM reference (Fig. 5) show that the magnitude of differences increases with increasing bond polarity, confirming that the strength of the bonding effect scales directly with the degree of net charge transfer.

For HAADF-STEM imaging, a useful parameter for characterizing depth-dependent imaging is the contrast signal as a function of depth, $C(z)$, defined here as the ratio of the HAADF intensity on a column with atomic number Z_1 to that on a column with atomic number Z_2 in a multielement crystal with $Z_1 > Z_2$: $C(z) = I_{Z_1}(z)/I_{Z_2}(z)$. By utilizing quantitatively calibrated STEM imaging, this value can be used to analyze both computational and experimental imaging. By considering the contrast signal as a function of depth (Fig. 6) for a 25 mrad 200 keV probe in AlN and NaF crystals, the effect of bonding model on HAADF images is captured simply.

As with x-z profiles, contrast signal comparisons benefit from normalization, showing the proportional effect of bonding relative to the IAM signal at any given depth as the percentage, $\{(C_{\text{bonded}} - C_{\text{IAM}})/C_{\text{IAM}}\} \times 100\%$. Normalized comparisons across six polar crystals (Fig. 7) show that beyond a depth of 20 nm, differences of 5%–25% relative to IAM are observed for BCM models, while differences range 5%–90% for FIM models. The contrast signal decreases

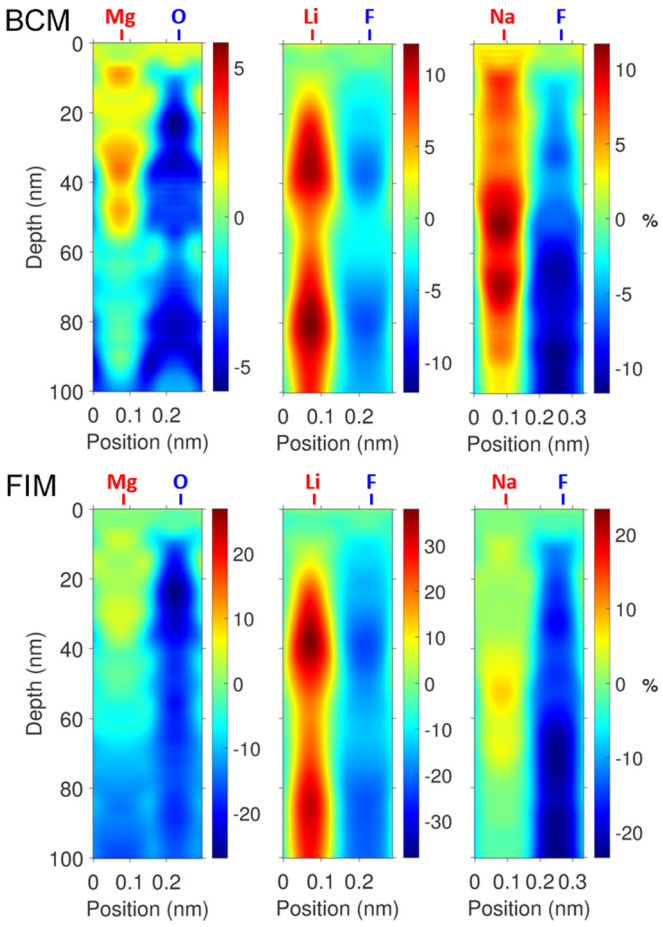

FIG. 4. (Color online) Normalized HAADF x-z profile differences of (a) BCM and (b) FIM bonding models relative to IAM reference, for ⟨110⟩-oriented halite crystals. Crystals increase in polarity from left to right. BCM vs IAM differences are weaker than FIM vs IAM.

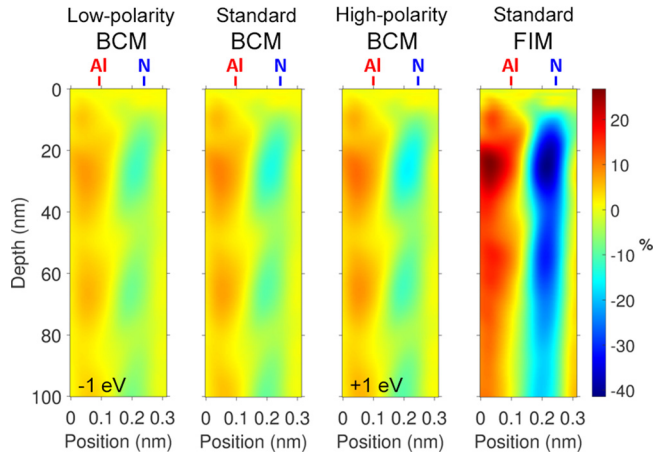

FIG. 5. (Color online) Normalized HAADF x-z profile differences for ⟨$\bar{2}$110⟩-oriented AlN with increasing charge transfer between Al and N from left to right: low polarity BCM model (electron potential energy on Al artificially lowered by 1 eV), standard BCM model, high-polarity BCM model (electron potential energy on Al artificially increased by 1 eV), and standard FIM model. As charge transfer between columns increases, normalized x-z profile differences for ⟨$\bar{2}$110⟩-oriented AlN reveal proportional strengthening of Al column intensity and weakening of N column intensity.

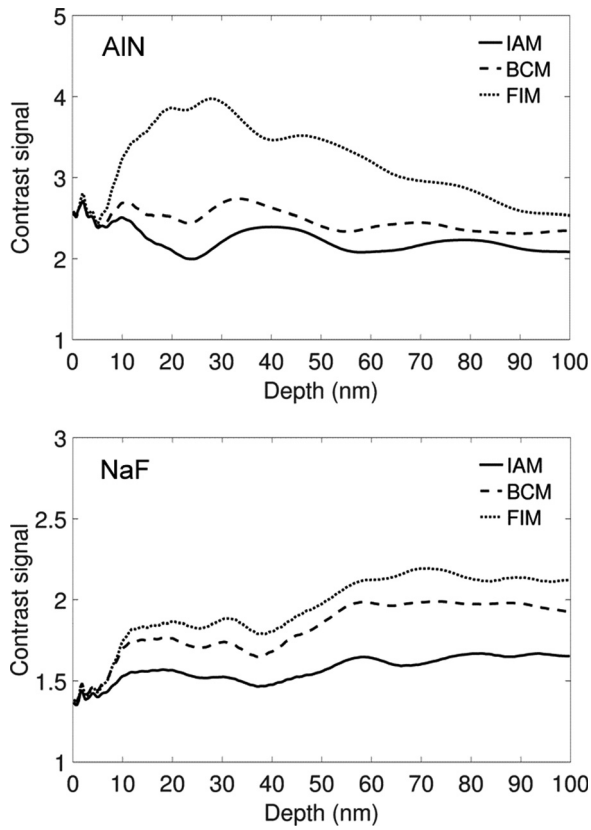

FIG. 6. Contrast signal for a 100 keV probe with 25 mrad convergence in ⟨$\bar{2}$110⟩-oriented AlN and ⟨110⟩-oriented NaF. The contrast signal varies both as a function of depth and bonding model. When the difference in Z is larger, the contrast signal is larger and varies more widely as a function of depth.

relative to the IAM model when the cation is lower in Z than the anion, whereas it increases when the cation is comparatively higher in Z. This is due to bonding-enhancement of cation column HAADF intensity and bonding-attenuation of anion column HAADF intensity.

B. Beam propagation

In view of the depth-dependent bonding effects on HAADF-STEM imaging considered above, simulations of STEM beam propagation are informative for understanding the influence of channeling and beam spreading on image contrast. Examples of such simulations for a 100 keV probe with 25 mrad convergence centered on the N column in ⟨$\bar{2}$110⟩-oriented AlN are plotted in Fig. 8. These plots simultaneously illustrate the fluctuation of intensity on the center N column and coupling of the beam to the nearest-neighboring Al column 0.11 nm away. Use of a single color-map scaling highlights changes introduced by polar bonding: as charge transfer increases, the intensity on the anionic N column decreases, the interaction between N and Al columns weakens, and the frequency of intensity fluctuations between Al and N columns increases. This manner of charge-transfer-dependent interaction affects all modes of STEM imaging, including even the HAADF-STEM mode discussed above.

When the probe is centered on a given atomic column, tracking the intensity on that column and its nearest

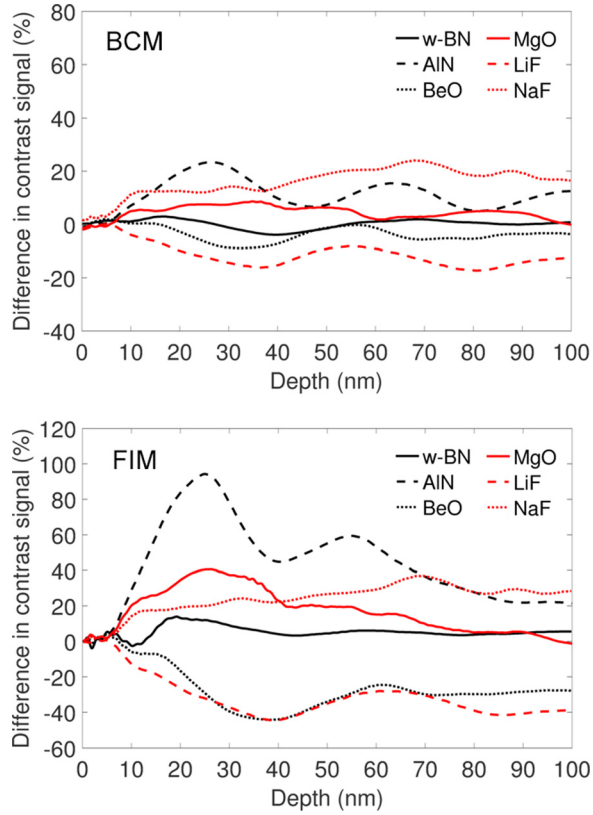

FIG. 7. (Color online) Change in HAADF contrast signal as a function of depth relative to IAM for a 100 keV probe with 25 mrad convergence. Effect of bonding on contrast is stronger for FIM model than for BCM, and in either case maximum changes in contrast ratio emerge at thicknesses of 20 nm or greater.

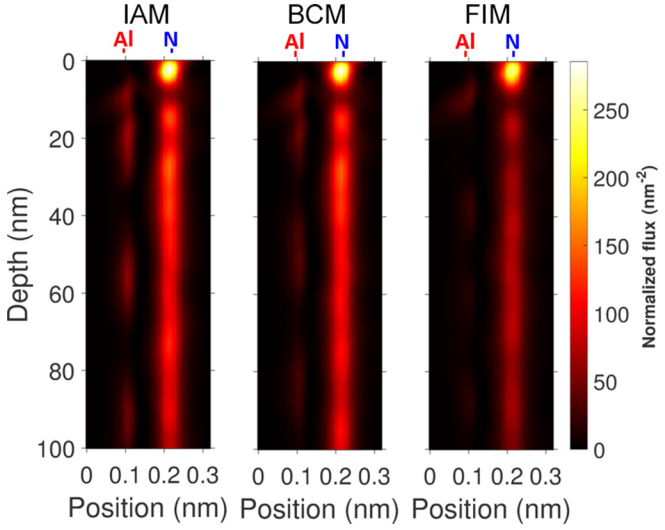

FIG. 8. (Color online) Intensity along line between nearest-neighboring columns in $\langle\bar{2}110\rangle$-oriented AlN as a function of depth, with incident 25 mrad 100 keV probe centered on the N column. Intensity fluctuates with thickness on the N column, but also couples to the neighboring Al column. Beam propagation visibly changes with bonding model.

neighboring columns reveals the origin of high-angle-scattered image intensity as a function of depth.[24,34] A systematic examination for a 100 keV probe with 25 mrad convergence show that $\langle\bar{2}110\rangle$-oriented wurtzite crystals (Fig. 9), $\langle 110\rangle$-oriented halite crystals (Fig. 10), and $\langle 100\rangle$-oriented diamond and zinc blende crystals (Fig. 11) all have both on-column channeling behavior and intercolumn beam spreading affected by polar bonding. As charge transfer increases, all cationic columns except Be increase the frequency and strength of on-column channeling while all anionic columns decrease the frequency and strength of on-column channeling; this contributes to the change in HAADF contrast signal, with HAADF intensity increasing on cation columns and decreasing on anion columns.

The coupling between incident and neighboring columns is strengthened by bonding for crystals with cation lower in Z than the corresponding anion; the same coupling is weakened by bonding when the cation is higher in Z than the anion. Intercolumn coupling has an especially strong effect on HAADF-STEM contrast for columns close (or far smaller) in Z than their neighbors, being so pronounced in some cases that the total intensity on neighboring columns is greater than that on the column where the probe was initially centered (e.g., centered on Li in LiF, Be in BeO, and either B or N in either phase of BN); with sufficient difference in Z this merely causes standard Z-contrast between the columns to be weakened, but in principle this can cause HAADF contrast reversals with two columns barely differing in Z. In polar crystals where this is an important consideration, this is the primary cause of bonding-dependent contrast changes: as intercolumn coupling decreases in strength due to bonding, contrast will either strongly increase (cation higher in Z than anion) or decrease (anion lower in Z than cation). In crystals with completely nonpolar bonding like d-C, including bonding does not meaningfully affect either on-column channeling or beam-spreading behavior, and thus does not affect HAADF-STEM imaging.

C. Incident probe effects

Many parameters of the incident electron probe may be varied while maintaining atomic resolution ADF imaging. Even with aberration-correction effectively canceling coherent aberrations to create a diffraction-limited probe, the probe energy, convergence angle, and finite source distribution all affect the beam-specimen interaction. Altered beam-specimen interaction, in turn, may alter the strength of bonding effects in ADF imaging.

By maintaining fixed convergence angle and changing beam energy, the effect of incident electron energy can be isolated. An example of beam energy effects is shown in Fig. 12 for HAADF imaging using 25 mrad probes for $\langle\bar{2}110\rangle$-oriented AlN, where increasing beam energy weakens the contrast change due to bonding and increases the period of depth-varying contrast fluctuations. Increasing electron energy reduces the wavelength of the electrons (reducing the probe size and "depth of focus" for a given convergence angle) and the phase shift due to elastic scattering. The finer probe size decreases intercolumn coupling strength and therefore the magnitude of contrast changes due to bonding; the smaller phase shift at higher energies

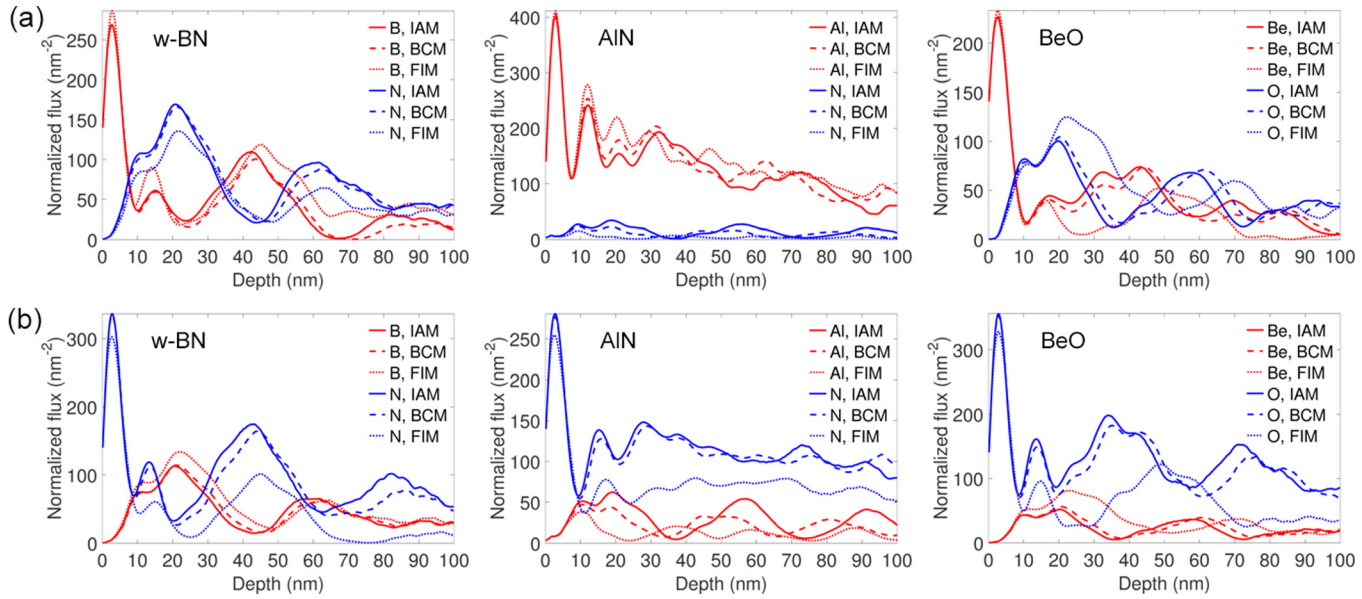

FIG. 9. (Color online) Probe intensity incident on atomic columns as a function of depth for $\langle\bar{2}110\rangle$-oriented wurtzite crystals, with incident probe centered on the (a) cation column and (b) anion column. Bond polarity increases from left to right. Intensity is tracked on incident columns, first-nearest-neighboring columns, and second-nearest-neighboring columns.

reduces the frequency of intercolumn intensity oscillations, in turn reducing the frequency of contrast fluctuations. These results show that the depth-dependence of bonding effects is critically sensitive to beam energy, and that even though bonding effects are slightly stronger at lower beam energies they are robustly present across a wide range of beam energies.

By maintaining fixed beam energy and changing convergence angle, the effect of changing convergence angle can likewise be isolated. An example of convergence angle effects is shown in Fig. 13 for HAADF imaging using 200 keV probes for $\langle\bar{2}110\rangle$-oriented AlN, where increasing convergence slightly weakens the contrast change due to bonding but does not alter the period of depth-varying contrast fluctuations. Increasing convergence angle reduces the probe size and "depth of focus" (for a given electron energy). The finer probe size decreases intercolumn coupling strength and therefore the magnitude of contrast changes due to bonding; because the phase shift due to elastic scattering remains the same, the frequency of contrast fluctuations is sensitive to bonding model but not convergence angle. This example shows that bonding effects are robustly observable

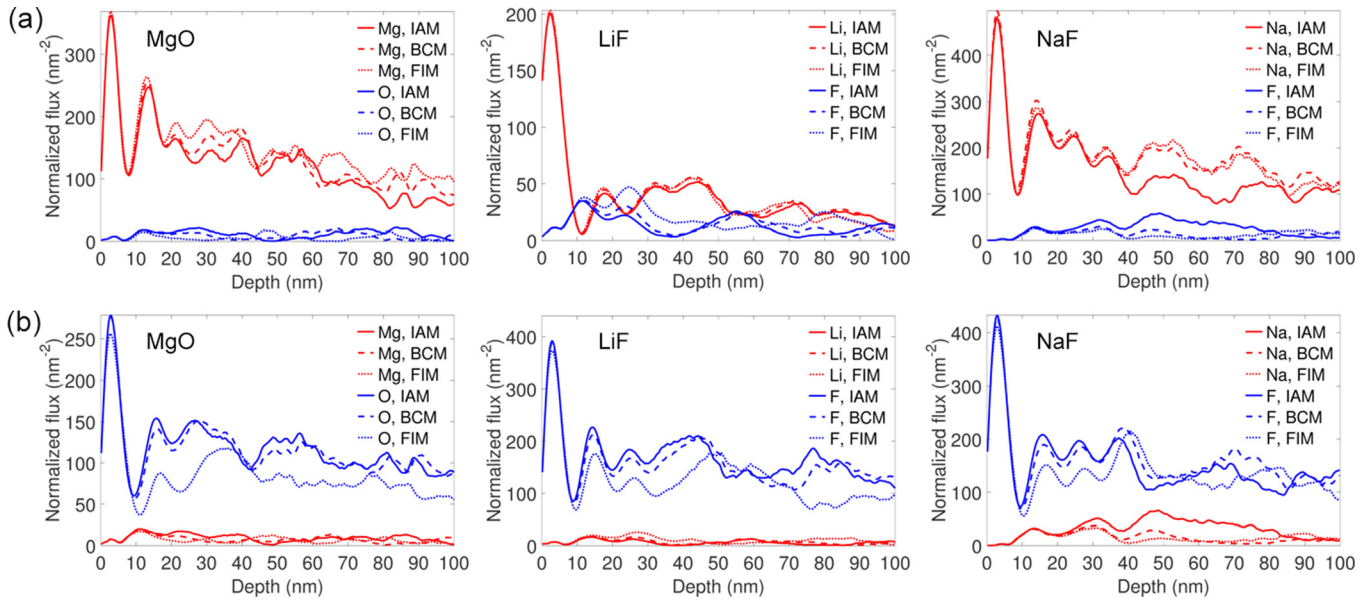

FIG. 10. (Color online) Probe intensity incident on atomic columns as a function of depth for $\langle 110\rangle$-oriented halite crystals, with incident probe centered on the (a) cation columns and (b) anion column. Bond polarity increases from left to right. Intensity is tracked on incident columns, first-nearest-neighboring columns, and second-nearest-neighboring columns.

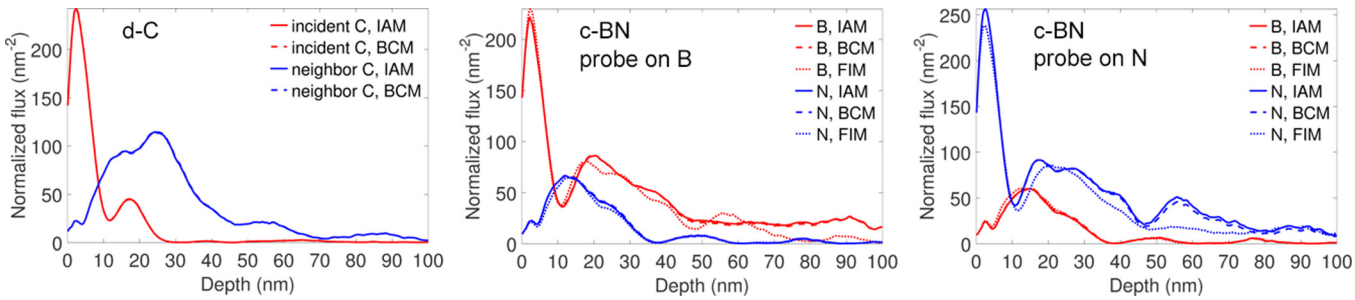

FIG. 11. (Color online) Probe intensity incident on atomic columns as a function of depth for ⟨100⟩-oriented cubic crystals, with incident probe centered on the (a) C column in d-C, (b) B column in c-BN, and (c) N column in c-BN. Bond polarity increases from left to right. Intensity is tracked on incident columns, first-nearest-neighboring columns, second-nearest-neighboring columns, and third-nearest-neighboring columns.

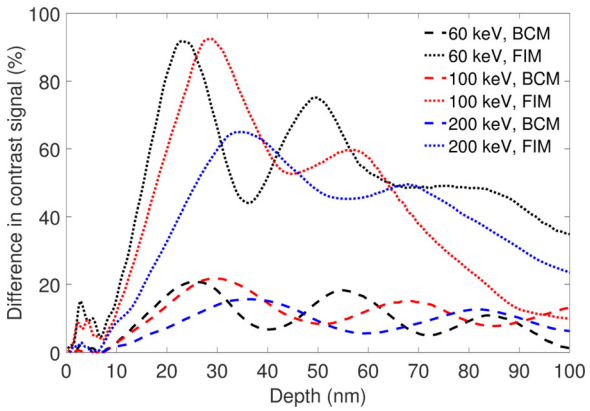

FIG. 12. (Color online) Change in contrast signal relative to IAM for 25 mrad probes imaging ⟨$\bar{2}$110⟩-oriented AlN, plotted as a function of depth, bonding model, and electron energy. With convergence angle fixed, the magnitude of contrast change decreases as probe energy increases. Also, the period of depth-dependent fluctuations in the contrast difference increases as probe energy increases.

over a wide range of convergence angles, and that this parameter would not need to be finely tuned to observe the effect experimentally.

A final critical factor to consider is that of finite source size, wherein the ideal diffraction-limited probe is incoherently blurred by the demagnified image of the source at the specimen. An example of finite source effects is shown in Fig. 14 for HAADF imaging using a 35 mrad 200 keV probe for ⟨$\bar{2}$110⟩-oriented AlN, where increasing the source size from a point source (effective probe FWHM 0.044 nm) to a gaussian with FWHM 0.05 nm (effective probe FWHM 0.067 nm) to a gaussian with FWHM 0.10 nm (effective probe FWHM 0.109 nm) weakens the contrast change due to bonding. Because the incoherent source contribution solely serves to blur the image, intensities are "flattened out" and contrast changes are reduced, but without contrast changes being altogether eliminated. This example demonstrates the benefit of imaging with highly bright sources and low beam currents to enable very fine demagnified source distributions at the specimen plane: the finer the source distribution, the stronger the change in contrast signal due to bonding. Also, because the quantitative effect of bonding on image contrast is very sensitive to the effective source distribution, it is

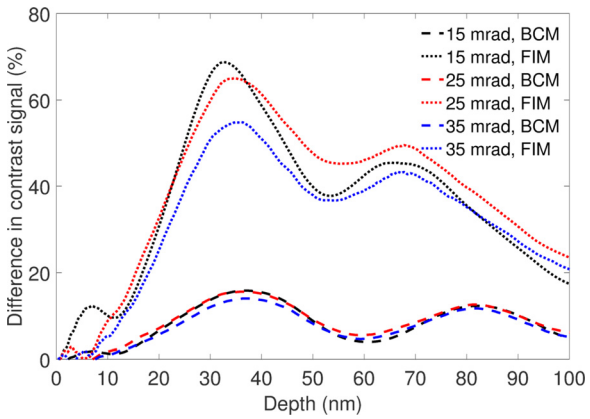

FIG. 13. (Color online) Change in contrast signal relative to IAM for 200 keV probes imaging ⟨$\bar{2}$110⟩-oriented AlN, plotted as a function of depth, bonding model, and convergence angle. With beam energy fixed, the magnitude of contrast change decreases as convergence angle increases. The period of depth-dependent fluctuations in the contrast difference does not change with convergence angle, only with bonding model.

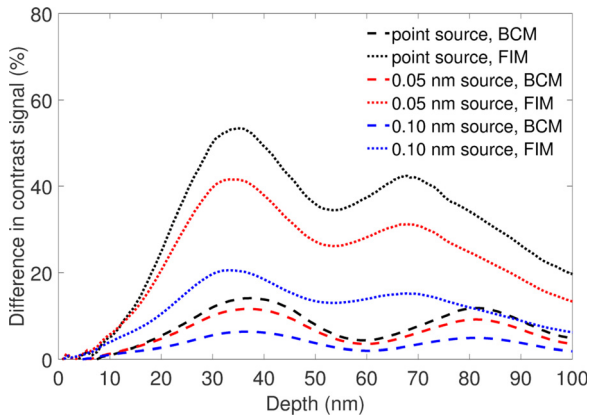

FIG. 14. (Color online) Change in contrast signal relative to IAM for 35 mrad 200 keV probes imaging ⟨$\bar{2}$110⟩-oriented AlN, plotted as a function of depth, bonding model, and source size. With convergence angle fixed, the magnitude of contrast change decreases as source size increases. The period of depth-dependent fluctuations in the contrast difference does not change with source size, only with bonding model.

critical to precisely determine the source distribution in any experiment seeking to measure the effect of bonding on ADF-STEM imaging.

D. Detector geometry effects

Although the focus thus far has been on "conventional" HAADF-STEM imaging—excluding any strong zero-order Laue zone scattering but collecting all higher-angle scattering including higher-order Laue zone rings—other modes of ADF-STEM imaging are also used for characterizing zone-axis-oriented crystals. Low-angle ADF (LAADF) STEM imaging, which excludes the bright-field disk but allows strong zero-order Laue zone scattering, is highly sensitive to strain fields in crystals and also allows for higher-efficiency (and thus lower-dose) imaging of thin, light-element crystals. Also, due to the complicating contributions of dynamical higher-order Laue zone diffraction in conventional HAADF-STEM imaging, it is instructive to consider "ultra-high-angle" ADF (UHAADF) STEM imaging that excludes first-order Laue zone rings to give "purer" Z-contrast.

For electron probes with 35 mrad convergence imaging $\langle\bar{2}110\rangle$-oriented AlN at multiple beam energies, the effects of detector geometry are surveyed in Fig. 15 for LAADF (40–200 mrad detector), HAADF (60–200 mrad detector), and UHAADF (200–500 mrad for 60 keV, 200–300 mrad for 100 keV, 150–200 mrad for 200 keV) geometries. The well-established effects of charge transfer, causing stronger contrast changes relative to IAM in the FIM model than the BCM model, are readily apparent for all detector geometries. Also, because coherent contributions to image intensity (zero-order and higher-order Laue zone scattering) do not depend strongly on channeling and beam spreading, contrast changes due to bonding increase from LAADF to HAADF to UHAADF detector geometries. It is interesting to note that the degree of splitting between LAADF, HAADF, and UHAADF contrast fluctuations depends on the beam energy, reflecting the complex effects of dynamical elastic scattering. The implications of these results is that detecting bonding effects is most readily done in highly incoherent ADF-STEM imaging modes, but can also be extended to LAADF-STEM. It should also be noted that the apparent higher effect on HAADF imaging modes versus LAADF is skewed by the method for calculating contrast: it is the ratio of the higher-Z column intensity to the lower-Z column intensity without background subtraction, placing LAADF images in a narrower contrast range than HAADF or UHAADF.

As noted previously for HAADF imaging, due to the weakening of elastic scattering (and thus also channeling effect magnitude) with the increase of beam energy, the magnitude of contrast changes decrease with increasing beam energy for all ADF geometries. Also, due to the decrease in the phase shift due to elastic scattering with the increase of beam energy, the depth frequency of contrast change fluctuations decreases with increasing beam energy, again for all ADF geometries. This demonstrates that bonding effects in ADF-STEM imaging are robust relative to changes in accelerating voltage, even though both the magnitude and frequency of bonding-induced contrast fluctuations depends on all details of the incident STEM probe and the detector geometry.

E. Thermal vibration effects

As alluded previously, TDS (Ref. 35)—a term encompassing the effects of atomic vibrations on the scattering of the TEM beam—makes an important contribution to quantitative prediction of the ADF-STEM contrast in typical imaging conditions.[36] Although other prominent TDS algorithms[24,36–38] exist, the following simulation results employ the frozen phonon[39] method, wherein images simulated using multiple thermally perturbed atomic configurations are incoherently averaged together. Owing to its robust treatment of both elastic scattering and dynamical TDS effects, the frozen phonon method has shown excellent agreement with experiment.[40] As is standard practice, atomic displacements were approximated by an isotropic Einstein model, neglecting the true anisotropy of phonon modes in crystals; including anisotropic phonon effects[41,42] would further improve the accuracy of bonding-inclusive multislice simulations, albeit to an unknown degree.

As explained in the methods, the TDS-inclusive simulations rely on a parameterized fitting of exact bonding-inclusive projected potentials; however, this adaptation causes these simulations to differ quantitatively from those used in the earlier sections of this study. The parameterized TDS-free simulations presented here are in principle

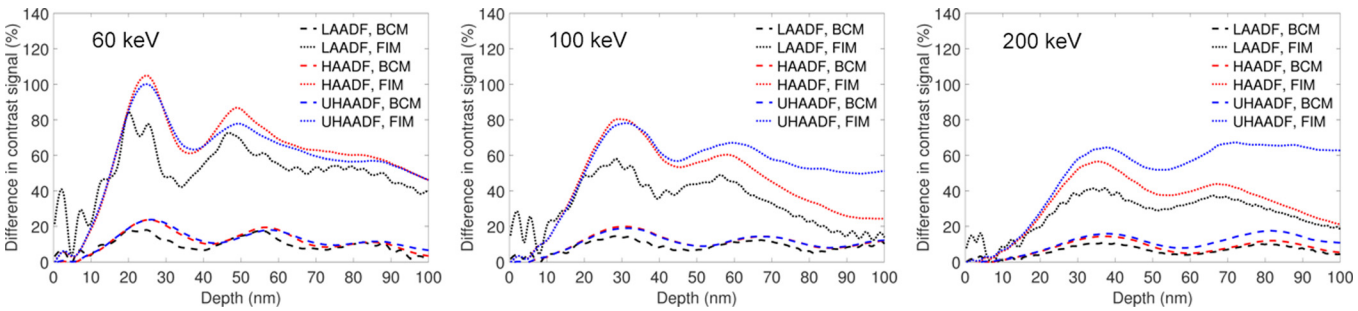

FIG. 15. (Color online) Change in contrast ratio relative to IAM for 35 mrad probes imaging $\langle\bar{2}110\rangle$-oriented AlN, plotted as a function of depth, bonding model, and detector geometry for (a) 60 keV, (b) 100 keV, and (c) 200 keV. Although all detectors collect high-angle-scattered electrons, decreasing the contribution of coherent beams from LAADF to HAADF to UHAADF settings strengthens the contrast fluctuations due to channeling and beam spreading effects.

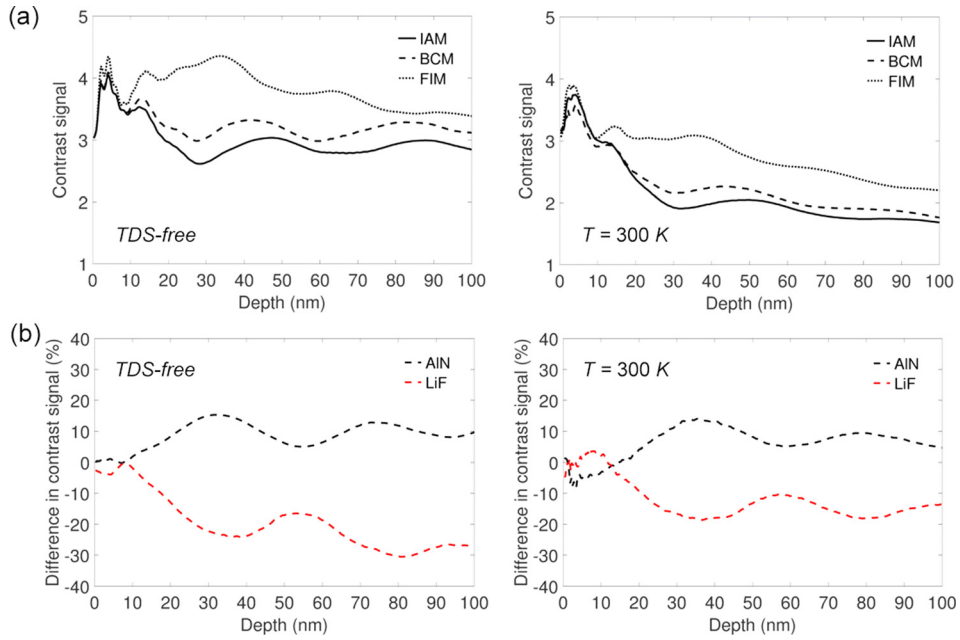

FIG. 16. (Color online) Examples of temperature effects on contrast, HAADF imaging using a 100 keV probe with 25 mrad convergence: (a) contrast signal plots for $\langle\bar{2}110\rangle$-oriented AlN with and without TDS, (b) differences in BCM vs IAM contrast signal for $\langle\bar{2}110\rangle$-oriented AlN and $\langle 110\rangle$-oriented LiF. TDS effects decrease image contrast for all bonding models, as well as perturb the contrast changes due to bonding.

equivalent to the exact simulations discussed in previous sections, but do not exhibit the same quantitative differences relative to IAM data as in the case of the exact projected potential inputs [e.g., for HAADF imaging using a 100 keV probe with 25 mrad convergence, the magnitude of maximum contrast signal difference for AlN is just over 20% and that for LiF is just under 20% in Fig. 7(a), but closer to 15% and 30%, respectively, Fig. 16(b)]. This may reflect inaccuracies in the fitting of the projected potentials, but also contains a contribution from the truncation of the potentials (maximum possible value of the projected potential is that at a half-pixel distance from the projected atomic position, with subpixel precision in the positioning of each randomly displaced atom) in the routine that calculates the projected potentials for each frozen phonon configuration using the fitting parameters. The calculation of exact projected potential inputs contained no such truncation and centered atoms exactly on pixels. The differences observed between results calculated with exact projected potential inputs and TDS-free parameterized inputs indicate that great care is required in adapting frozen phonon simulations to include bonding.

TDS serves to increase the overall intensity of an ADF-STEM image, introducing an increased "background" level and thus a decreased contrast signal, as shown in examples of HAADF simulations of AlN [Fig. 16(a)]. This seems to show that the strongest, most distinct effects of bonding are visible in crystals with no thermal vibrations. However, the differences in HAADF contrast signal for BCM relative to IAM [Fig. 16(b)] are very much preserved at 300 K, and remain comparable in magnitude to those in TDS-free simulation. These results show that bonding effects are not negated by the atomic vibrations and may be detected at room temperature; however, they also corroborate the necessity of including TDS for comparing simulations to room temperature experiments.

When the strength of TDS is increased, changing the configuration of atoms from fixed equilibrium positions in TDS-free case to moderate RMS displacements at liquid nitrogen temperatures (77 K) to double those RMS displacements at room temperature (300 K), contrast fluctuations for ADF-STEM imaging of $\langle\bar{2}110\rangle$-oriented AlN with a 25 mrad probe at 100 keV are only weakly influenced by temperature across detector geometries (Fig. 17). In this case, TDS

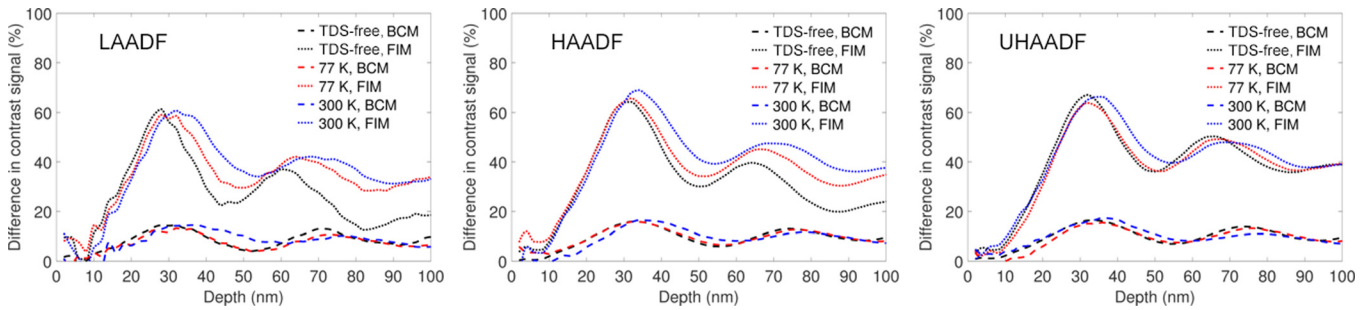

FIG. 17. (Color online) Examples of temperature effects on contrast: 100 keV probe with 25 mrad convergence for LAADF, HAADF, and UHAADF detectors. TDS effects slightly increase the magnitude of contrast fluctuations relative to IAM and slightly increase the period of these fluctuations.

actually increases the magnitude of contrast changes; this can be explained because TDS reduces the baseline contrast level, but since the strength of bonding effects is essentially unchanged by TDS the magnitude of normalized contrast fluctuations increases slightly. This example shows that, at least within this conventional temperature window, TDS only serves as a minor perturbation on the robust depth-dependent bonding effect, even serving to "enhance" it in some cases. Thus, experiments do not have to be performed at low temperatures to examine bonding effects, but can be performed at room temperature also.

IV. CONCLUSIONS

Versatile methods for adapting multislice simulations to include bonding have been presented. Exact transformation of charge densities calculated using each bonding model allows fundamental examination of bonding effects apart from thermal vibrations. The approximate fitting of the exact projected potentials removes some of the symmetry of bonding but preserves its charge transfer effects, allowing for physically realistic simulation of crystals including TDS effects represented by a frozen phonon model. These methods serve as reasonable means to perform multislice simulations without being constrained by the IAM approximation.

A survey of initial bonding-inclusive simulations reveals that polar bonding alters the channeling and beam spreading of focused STEM probes, which in turn alters the ADF-STEM imaging for any combination of incident probe, detector geometry, and material temperature; this is true even of the HAADF imaging mode, where coherent scattering contributions to detected intensity are minimized. Although effects of finite demagnified source size strongly dampen the effects of bonding on ADF-STEM image contrast, they do not erase it. These results suggest that ADF-STEM bonding effects should be experimentally measurable in a thoroughly characterized microscope. The effect on ADF image contrast should be most pronounced in crystals with large net charge transfer, under illumination with a very fine effective source size at the specimen.

In principle, the accuracy of ADF image and spectrum image analysis in polar crystals is always improved by including bonding; in practice, the effect may often be overwhelmed by typical uncertainties in thickness, surface damage effects, effective source distribution, defocus, and low-order aberrations. Nevertheless, in addition to refining the analysis of ideal single crystals, the inclusion of bonding effects may prove important for systems containing highly charged defects such as ordered point defects, dislocation cores, and polar interfaces.

ACKNOWLEDGMENTS

M.L.O. and K.A.M. acknowledge partial support by the NSF under Award No. DMR-1006706 and NSF MRSEC under Award No. DMR-1420013; M.L.O. also received support from the University of Minnesota Graduate School Fellowship. Multislice simulations and DFT calculations were performed using computational resources provided by the Minnesota Supercomputing Institute at the University of Minnesota. Aloysius Gunawan and Anudha Mittal provided helpful insight in discussions.

[1]J. M. Cowley and A. F. Moodie, Acta Crystallogr. **10**, 609 (1957).
[2]M. A. O'Keefe, P. R. Buseck, and S. Iijima, Nature **274**, 322 (1978).
[3]E. J. Kirkland, R. F. Loane, and J. Silcox, Ultramicroscopy **23**, 77 (1987).
[4]J. M. Zuo, P. Blaha, and K. Schwarz, J. Phys.: Condens. Matter **9**, 7541 (1997).
[5]J. Zuo, Mater. Trans., JIM **39**, 938 (1998).
[6]J. M. Zuo, M. Kim, M. O'Keeffe, and J. C. H. Spence, Nature **401**, 49 (1999).
[7]B. Deng and L. D. Marks, Acta Crystallogr. A **62**, 208 (2006).
[8]J. Ciston, J. S. Kim, S. J. Haigh, A. I. Kirkland, and L. D. Marks, Ultramicroscopy **111**, 901 (2011).
[9]J. C. Meyer *et al.*, Nat. Mater. **10**, 209 (2011).
[10]N. Shibata, S. D. Findlay, Y. Kohno, H. Sawada, Y. Kondo, and Y. Ikuhara, Nat. Phys. **8**, 611 (2012).
[11]K. Muller *et al.*, Nat. Commun. **5**, 5653 (2014).
[12]J. M. Cowley, Ultramicroscopy **2**, 3 (1976).
[13]S. Pennycook, Ultramicroscopy **30**, 58 (1989).
[14]S. Pennycook and L. Boatner, Nature **336**, 565 (1988).
[15]M. Haider, S. Uhlemann, E. Schwan, H. Rose, B. Kabius, and K. Urban, Nature **392**, 768 (1998).
[16]P. E. Batson, N. Dellby, and O. L. Krivanek, Nature **418**, 617 (2002).
[17]P. D. Nellist *et al.*, Science **305**, 1741 (2004).
[18]R. Erni, M. D. Rossell, C. Kisielowski, and U. Dahmen, Phys. Rev. Lett. **102**, 096101 (2009).
[19]J. Fertig and H. Rose, Optik **59**, 407 (1981).
[20]R. F. Loane, E. J. Kirkland, and J. Silcox, Acta Crystallogr. A **44**, 912 (1988).
[21]A. Mittal and K. A. Mkhoyan, Ultramicroscopy **111**, 1101 (2011).
[22]S. Hillyard, R. F. Loane, and J. Silcox, Ultramicroscopy **49**, 14 (1993).
[23]K. Ishizuka, J. Electron Microsc. **50**, 291 (2001).
[24]L. J. Allen, S. D. Findlay, M. P. Oxley, and C. J. Rossouw, Ultramicroscopy **96**, 47 (2003).
[25]L. F. Kourkoutis, M. K. Parker, V. Vaithyanathan, D. G. Schlom, and D. A. Muller, Phys. Rev. B **84**, 075485 (2011).
[26]J. Etheridge, S. Lazar, C. Dwyer, and G. A. Botton, Phys. Rev. Lett. **106**, 160802 (2011).
[27]D. M. Smyth, Annu. Rev. Mater. Sci. **15**, 329 (1985).
[28]H. Y. Hwang, Y. Iwasa, M. Kawasaki, B. Keimer, N. Nagaosa, and Y. Tokura, Nat. Mater. **11**, 103 (2012).
[29]E. Kirkland, *Advanced Computing in Electron Microscopy* (Springer, New York, 2010).
[30]P. Giannozzi *et al.*, J. Phys.: Condens. Matter **21**, 395502 (2009).
[31]J. P. Perdew, K. Burke, and M. Ernzerhof, Phys. Rev. Lett. **77**, 3865 (1996).
[32]W. Kohn and L. J. Sham, Phys. Rev. **140**, A1133 (1965).
[33]P. P. Ewald, Ann. Phys. **369**, 253 (1921).
[34]C. Dwyer and J. Etheridge, Ultramicroscopy **96**, 343 (2003).
[35]C. R. Hall and P. B. Hirsch, Proc. R. Soc. London, A **286**, 158 (1965).
[36]Z. L. Wang and J. M. Cowley, Ultramicroscopy **31**, 437 (1989).
[37]C. Fanidis, D. Van Dyck, and J. Van Landuyt, Ultramicroscopy **48**, 133 (1993).
[38]B. D. Forbes, A. V. Martin, S. D. Findlay, A. J. D'Alfonso, and L. J. Allen, Phys. Rev. B **82**, 104103 (2010).
[39]R. F. Loane, P. Xu, and J. Silcox, Acta Crystallogr., A **47**, 267 (1991).
[40]J. M. LeBeau, S. D. Findlay, L. J. Allen, and S. Stemmer, Phys. Rev. Lett. **100**, 206101 (2008).
[41]D. A. Muller, B. Edwards, E. J. Kirkland, and J. Silcox, Ultramicroscopy **86**, 371 (2001).
[42]A. V. Martin, S. D. Findlay, and L. J. Allen, Phys. Rev. B **80**, 024308 (2009).